PAPER

Location effects of vanadium in NiFe layered double hydroxides for oxygen evolution reaction†

Mengze Ma, Yechi Zhang, Xiaoqian Ding, Jianlei Jing, Linbo Jin, Wei Liu, Daojin Zhou [ID] * and Xiaoming Sun [ID] *

NiFe layered double hydroxides (NiFe-LDHs) have been widely acknowledged as a promising anode electrocatalyst in alkaline oxygen evolution reactions (OERs), and vanadium has demonstrated its capability to improve their OER performance. Considering that V can exist as three vanadium-based species, *i.e.*, doped V^{III} in LDH laminates, intercalated VO_3^- between LDH interlayers, and free VO_3^- as an additive in KOH electrolyte, we systematically studied and compared their effects in determining the OER performance of NiFe-LDHs. Electrochemical results reveal that all three conditions mentioned above individually can improve the OER performance of NiFe-LDHs. When two of these conditions are present at the same time, the combination of VO_3^- intercalated into LDHs as the catalyst and free VO_3^- as the additive in KOH electrolyte shows the best OER performance, even exceeding the performance exhibited by the combination of all three conditions. *Ex situ* Raman results indicate that VO_3^- intercalation triggers an active γ-phase formation of NiFe-LDHs; *in situ* Raman data further reveal that VO_3^- as an electrolyte additive stabilizes this active phase and slows down the dissolution of LDHs, as supported by inductively coupled plasma characterization.

Introduction

Renewable energy-powered hydrogen production by water electrolysis is one of the most effective approaches to realize carbon neutrality.[1] In comparison with hydrogen evolution reaction (HER) at the cathode, oxygen evolution reaction (OER) at the anode encounters high overpotential and the catalysts suffer from easy oxidation and severe degradation.[2] In recent years, to overcome this barrier, researchers have devoted considerable efforts to improve the activity and stability of OER electrocatalysts.[3] Many materials have been used for OER, such as perovskites,[4] metal–organic frameworks[5] and layered double hydroxides (LDHs).[6] Transition metal-based LDHs have been proved by many studies to have great prospect in OER, especially the nickel–iron LDHs.[7] The compositional modulation of their laminates[8] and exchangeable intercalated anions[9] further hold promise of advancing the OER performance. In terms of the intercalation anion, Zhou *et al.* intercalated sixteen species of anions into NiFe LDHs and found out that the OER activity by these LDHs shows a linear correlation with the standard redox potential of intercalated anions.[10] Regarding the doping element of the laminates, various transition metals have been tried. Zhao *et al.* induced high-valence Zr^{4+} into NiFe hydroxide,

State Key Laboratory of Chemical Resource Engineering, Beijing University of Chemical Technology, Beijing 100029, China. E-mail: zhoudj@mail.buct.edu.cn; sunxm@mail.buct.edu.cn

gaining a lower overpotential at 10 mA cm^{-2} and a faster current rising rate.[11] These are attributed to the optimized Fe active sites after doping Zr^{4+}. Duan *et al.* doped NiFe-LDH with tungsten using a simple one-step alcohothermal method.[12] Compared with non-doped NiFe-LDH, the iron in NiFeW-LDH rises to a higher valence, resulting in more active intermediates to attach to Fe and the acceleration of the rate-determining step.

Among all transition metals, vanadium as the third doping metal in NiFe-LDHs is a special one. As an early-transition metal, V cation has abundant empty d orbitals. Chen *et al.* synthesized Ni/Fe/V ternary layered double hydroxides by the one-pot method.[13] By regulating the doping amount of vanadium on the LDH laminates, the electrical conductivity can be optimized to obtain the most suitable adsorption energy of the active species in OER, resulting in accelerated four-step electron transfer. Since vanadium belongs to the same period as nickel and iron, a similar cation radius makes it easier to be doped into NiFe-LDHs. On the other hand, as a muti-valent metal, vanadium has many oxysalts, among which metavanadate is stabilized as the hydrated ion in the alkaline solution. When vanadium exists in the electrolyte in the form of the metavanadate anion, it will be absorbed on the anode catalyst surface by electrostatic force, which may also affect the performance of OER.

In this work, we used NiFe-LDHs powder as a model catalyst to investigate the effects from the following three categories: doped vanadium (V^{III}) in NiFe-LDHs laminates, intercalated metavanadate (VO_3^-) in the interlayer space, free VO_3^- as an

This journal is © The Royal Society of Chemistry 2024

J. Mater. Chem. A, 2024, **12**, 23447–23453 | **23447**

additive in KOH anolyte (Fig. 1a). A systematic summary and comparison of the corresponding OER performance shows that all the conditions existing alone can promote the OER performance. When two or three strategies work simultaneously in OER, the combination of VO_3^- intercalated NiFe-LDHs in the presence of 0.32 mM VO_3^- in the anolyte shows the best property. The XRD and Raman results indicate that VO_3^- in the interlayer space and anolyte contributes to the fast transformation of NiFe-LDHs into a γ-NiOOH phase, which accounts for the high OER activity and maintains this phase during operation against further evolution or degradation.

Result and discussion

Using a co-precipitation method, we prepared a series of LDHs with Ni/Fe ratio of 2:1 and intercalated them by traditional CO_3^{2-} (CO_3^{2-}-Ni_2Fe_1LDHs) and VO_3^- (VO_3^--Ni_2Fe_1LDHs) (see details in the Experimental section, Fig. 1b shows the schematic diagram of the preparation process of VO_3^--Ni_2Fe_1LDHs as an example). The comparison of the transmission electron microscopy (TEM) images in Fig. 1c and d shows that the VO_3^--Ni_2Fe_1LDHs have a smaller size distribution and a looser nanostructure than CO_3^{2-}-Ni_2Fe_1LDHs. The X-ray diffraction (XRD) patterns (Fig. 1e) show that the two samples are in good accordance with the NiFe-LDHs (JCPDF: 40-0125), but the (003) and (006) peaks of CO_3^{2-}-Ni_2Fe_1LDHs are sharper than those of VO_3^--Ni_2Fe_1LDHs, indicating its well-ordered crystalline structure and a larger lateral size (in agreement with the TEM data).

Furthermore, we also noticed the (003) diffraction peak shift towards a lower angle in the VO_3^--Ni_2Fe_1LDHs, which can be attributed to a larger radius of intercalated VO_3^- compared to CO_3^{2-} (Fig. S1, and ESI†). Later on, we tested the elemental composition of the powder samples by inductively coupled plasma optical emission spectrometry (ICP-OES), verifying that the molar ratio of Ni/Fe of the as-prepared samples is consistent with the feeding ratio (Table S1, and ESI†). The change of the intercalated anion brings an excellent OER improvement, which is shown in Fig. S2a.† The electrochemical results demonstrate that the overpotential at 10 mA cm^{-2} decreases from 353 mV using CO_3^{2-}-Ni_2Fe_1LDHs as the OER electrode to 258 mV when VO_3^--Ni_2Fe_1LDHs is employed as a working electrode. Subsequently, X-ray photoelectron spectroscopy (XPS) was used to characterize the Ni/Fe valence state (Fig. S2b and c†). The Ni 2p as well as Fe 2p spectra exhibit two contributions, $2p_{3/2}$ and $2p_{1/2}$ (resulting from the spin–orbit splitting). We find that after changing the intercalated anion from CO_3^{2-} to VO_3^-, the binding energy of Ni $2p_{3/2}$ increases slightly (855.65 eV to 855.73 eV) along with the B.E. of Fe $2p_{3/2}$, which decreases (712.30 eV to 712.13 eV), indicating that the valence of Ni (Fe) in VO_3^--Ni_2Fe_1LDHs is higher (lower) than that in CO_3^{2-}-Ni_2Fe_1LDHs. All the long-term stability tests of the samples were carried out at 80 °C, under a constant current density of 400 mA cm^{-2}, in the two-electrode system. The data is shown in Fig. S5a.†

The blue bars represent the average voltage during the stability test of LDHs. Apparently, even the lowest voltage of CO_3^{2-}-Ni_2Fe_1LDHs (3.1 V) is higher than the highest voltage of
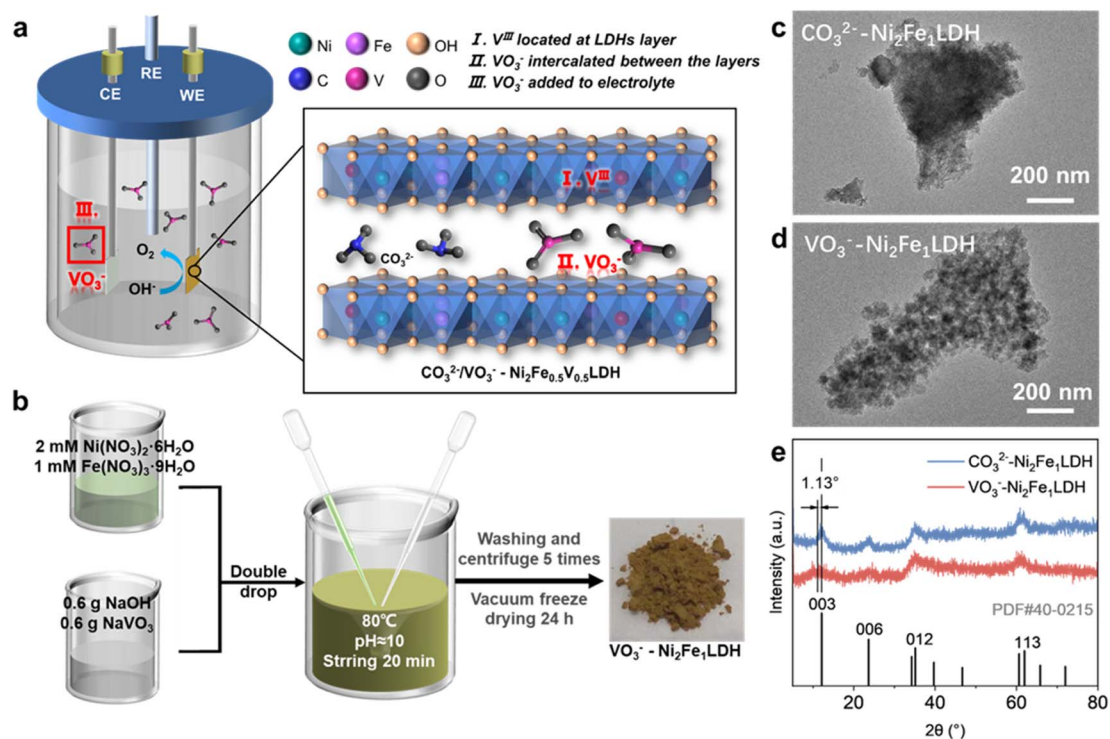

Fig. 1 (a) Schematic diagram of three locations of V species in a water splitting system using NiFe-LDHs as the anode, (b) schematic diagram of the co-precipitation method (take VO_3^--Ni_2Fe_1LDHs for example), TEM images of (c) CO_3^{2-}-Ni_2Fe_1LDHs and (d) VO_3^--Ni_2Fe_1LDHs, (e) XRD spectra of CO_3^{2-}-Ni_2Fe_1LDHs and VO_3^--Ni_2Fe_1LDHs.

23448 | *J. Mater. Chem. A*, 2024, **12**, 23447–23453

This journal is © The Royal Society of Chemistry 2024

VO_3^--Ni_2Fe_1LDHs (2.7 V). Compared with the starting voltage and ending voltage, VO_3^--Ni_2Fe_1LDHs with electrolysis addition concentration at 0.32 mM show the lowest decay after the stability test. Comparing both the activity and stability data above, we find that when the electrolyte combination is 1 M KOH + 0.32 mM $NaVO_3$, VO_3^--Ni_2Fe_1LDHs present an optimal OER performance.

Then, the effect of V^{III} doping in LDHs laminates on the OER performance was studied. After synthesizing five ratios of Ni_2-$Fe_xV_{(1-x)}$LDHs, the activity and stability were tested in 1 M KOH. When the ratio of Fe/V reaches 0.5/0.5, the best activity of OER is obtained. The overpotential of $Ni_2Fe_{0.5}V_{0.5}$LDHs at 10 mA cm^{-2} is only 306 mV (Fig. S6†). Then, the stability test also showcases that this sample is the most stable candidate (Fig. S7†).

After conducting the aforementioned three sets of experiments, we observed that the simultaneous presence of VO_3^- in the interlayer and electrolyte or doping V^{III} in LDHs all resulted in improved activity and stability; thus, we synthesized VO_3^--$Ni_2Fe_{0.5}V_{0.5}$LDHs and subjected it to testing at 1 M KOH with varying concentrations of VO_3^- (Fig. S8†).

Fig. 2b summarizes the overpotential at 10 mA cm^{-2} according to the CV curves from Fig. 2a, S4, S6 and S8.† Also, the relevant specific value of the OER activity and durability is shown in Table S2.† For CO_3^{2-}-Ni_2Fe_1LDHs, it is easier to find that along with the increase in the additive $NaVO_3$, the overpotential decreases. When the concentration of VO_3^- reaches 0.48 mM, the overpotential no longer changes, indicating that the enhancement brought by additive reaches its maximum (overpotential decreases 13 mV). When the electrolyte consists of 1 M KOH + 0.32 mM $NaVO_3$, the lowest overpotential for VO_3^--Ni_2Fe_1LDHs was achieved at 234 mV (119 mV decreased compared with the reference sample), showcasing the best activity among all the samples. Also, the lowest overpotential drop brought by doping vanadium on laminates is 50 mV compared with the reference sample at the best Fe : V ratio (0.5 : 0.5). The activity of VO_3^--$Ni_2Fe_{0.5}V_{0.5}$LDH represented by a green line is inferior than that of VO_3^--Ni_2Fe_1LDHs, presenting a 30 mV higher overpotential. Subsequently, we selected the best combination of the three groups (that is, catalyst VO_3^--Ni_2Fe_1LDHs with VO_3^- concentration at 0.32 mM, $Ni_2Fe_{0.5}$-$V_{0.5}$LDHs with no VO_3^- and VO_3^--$Ni_2Fe_{0.5}V_{0.5}$LDHs with VO_3^- concentration at 0.64 mM) and CO_3^{2-}-Ni_2Fe_1LDHs with no VO_3^- as the reference sample to obtain the CV curves. Fig. S10† illustrates the C_{dl} values for these four LDHs as well as the voltage–current diagrams after electrochemically active surface area (ECSA) normalization. It can be concluded that normalized activity follows similar trends as that before normalization, suggesting the excellent intrinsic activity of VO_3^--Ni_2Fe_1LDHs. The long-term stability tests results are shown in Fig. 2e, and the average voltage along with voltage decay during stability testing are summarized in Fig. 2d. Among all the samples, VO_3^--Ni_2Fe_1LDHs tested in 1 M KOH + 0.32 mM $NaVO_3$ exhibited the lowest average voltage (2.70 V), delivering the best OER activity and stability.

The OER activity and stability of VO_3^--$Ni_2Fe_{0.5}V_{0.5}$LDHs in the electrolyte containing VO_3^- were found to not have the expected performance; thus, we focus on the case of VO_3^- as the

intercalated anions and electrolyte additives in subsequent investigations. The stability test was conducted at room temperature at a current density of 50 mA cm^{-2} for 50 hours (Fig. S11†), and XRD and XPS analyses were performed on the working electrodes before and after the stability test. As observed from the XRD analysis in Fig. S12,† after the stability test, there is a shift in the peak position for CO_3^{2-}-Ni_2Fe_1LDHs from 12.04° to a lower angle of 11.80°, indicating an increase in the interlayer spacing. On the other hand, for VO_3^--Ni_2Fe_1-LDHs, there is a shift in the peak position from 10.44° to a higher angle of 11.87°, suggesting a decrease in the interlayer spacing. Applying Bragg's equation ($2d \sin \theta = n\lambda$, $\lambda = 0.15406$ nm), it can be calculated that the interlayer distance expands from 7.34 Å to 7.49 Å for CO_3^{2-}-Ni_2Fe_1LDHs, while it decreases from 8.46 Å to 7.49 Å for VO_3^--Ni_2Fe_1LDHs. The changes observed through XRD indicate that both CO_3^{2-}-Ni_2Fe_1LDHs and VO_3^--Ni_2Fe_1LDHs undergo a phase transformation after the long-term stability test, CO_3^{2-}-Ni_2Fe_1LDHs expands the layer spacing while VO_3^--Ni_2Fe_1LDHs narrows down. Based on the four proposed Bode models by Strasser *et al.* regarding Ni(II/III) hydroxide transformation,[14] we speculate that before the stability test, both CO_3^{2-}-Ni_2Fe_1LDHs and VO_3^--Ni_2Fe_1LDHs are β-Ni(OH)$_2$ phases. But the phase change during the OER requires further studies.

The XPS of the two LDHs was performed after the stability test, and the results are presented in Fig. 3a and b. The binding energies of the Ni $2p_{3/2}$ peak are summarized in Fig. 3c upper graph. Firstly, the Ni valence of VO_3^--Ni_2Fe_1LDHs is higher than that of CO_3^{2-}-Ni_2Fe_1LDHs. According to the model proposed by Strasser,[14] γ-NiOOH has a Ni valence range of 3.5–3.7, while β-NiOOH has a Ni valence of about 3.0. This evidence qualitatively verifies that there are two distinct phases between CO_3^{2-}-Ni_2-Fe_1LDHs and VO_3^--Ni_2Fe_1LDHs. Secondly, compared to CO_3^{2-}-Ni_2Fe_1LDHs, VO_3^--Ni_2Fe_1LDHs exhibits less increase in the nickel valence state after stability testing, suggesting that the VO_3^--Ni_2Fe_1LDHs sample itself is closer to the stable active phase with minimal changes in its valence state and lattice spacing throughout the test period. Lastly, by comparing the average voltage calculated in Fig. 3c bottom graph, it was observed that there is a close correlation between the average voltage and nickel valence state fluctuations. For CO_3^{2-}-Ni_2-Fe_1LDHs, both the nickel valence state and average voltage exhibit significant variation ranges; they initially decreased, followed by an increase, until reaching maximum stability when 0.32 mM VO_3^- was present in the electrolyte solution, while for VO_3^--Ni_2Fe_1LDHs, both the nickel valence state and voltage show minor variations, indicating that intercalation of VO_3^- assists in maintaining a more stable nickel valence state, resulting in less changes in the voltage due to external factors (in this case: the concentration of VO_3^- in the electrolyte).

The concentration of Ni and Fe cations dissolved from the catalyst during the 50 h stability test is shown in Fig. 3d. Regardless of the type of the catalyst, the dissolution of Fe initially decreases and then increases while the dissolution of Ni uniformly decreases with an increase in the VO_3^- concentration in the electrolyte. Moreover, it is evident that the presence of VO_3^- results in a significantly smaller amount of Ni/Fe
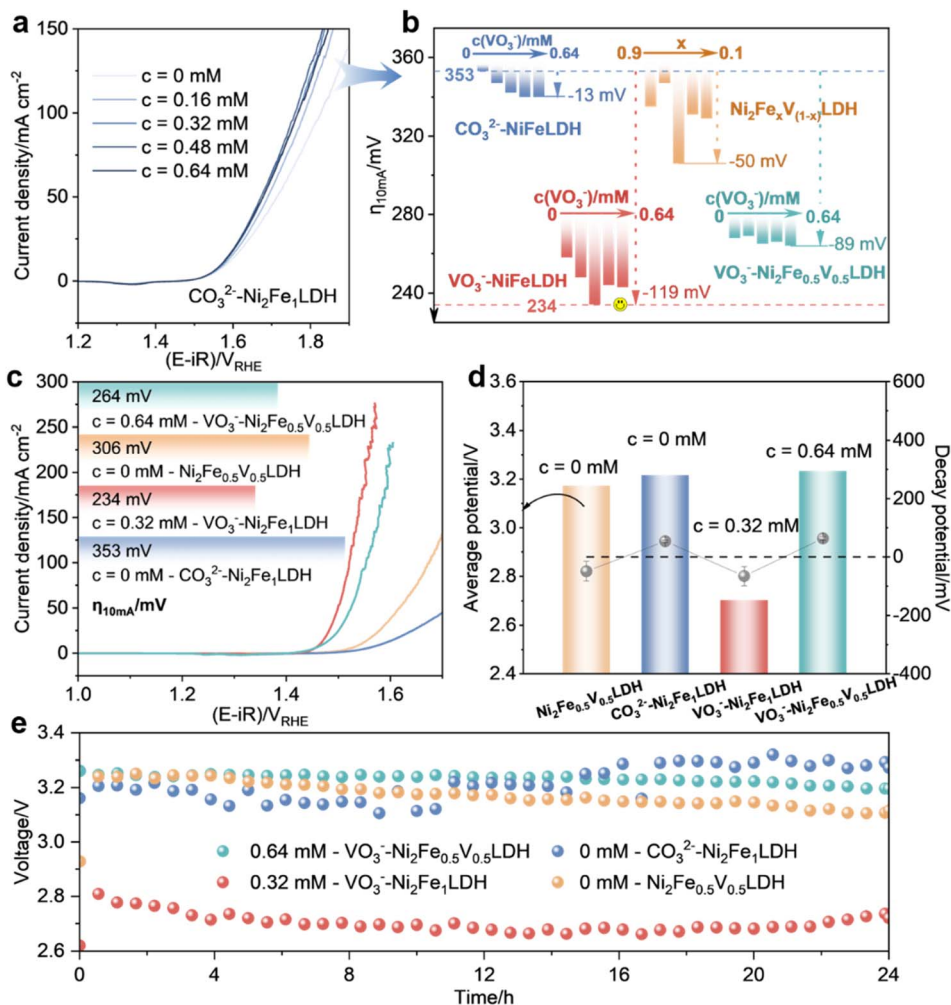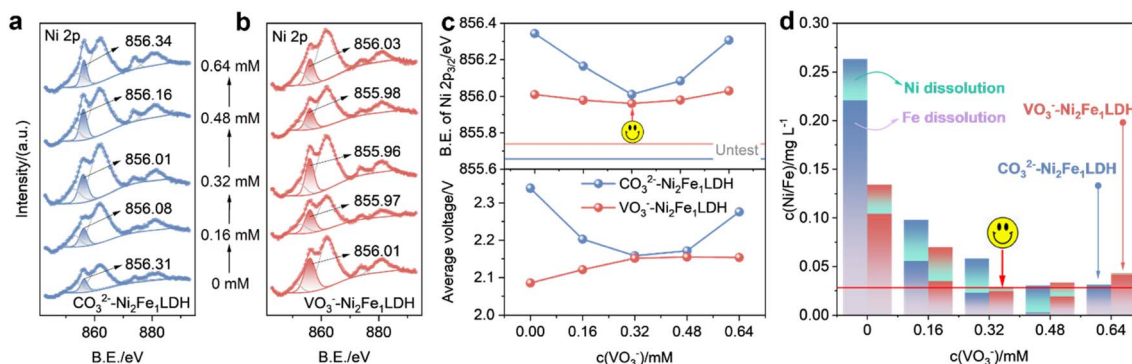
This journal is © The Royal Society of Chemistry 2024

J. Mater. Chem. A, 2024, **12**, 23447–23453 | **23449**

Fig. 2 (a) Cyclic voltammetry (CV) curve of CO_3^{2-}–Ni_2Fe_1LDHs in 1 M KOH + c mM $NaVO_3$, respectively, scan rate of CV is 5 mV s^{-1}, (b) summary chart of overpotentials at 10 mA cm^{-2} of CO_3^{2-}–Ni_2Fe_1LDHs-catalyzed OER in 1 M KOH + c mM $NaVO_3$ (blue line), VO_3^-–Ni_2Fe_1LDHs-catalyzed OER in 1 M KOH + c mM $NaVO_3$ (red line), $Ni_2Fe_xV_{(1-x)}$LDHs-catalyzed OER in 1 M KOH (yellow line), VO_3^-–$Ni_2Fe_{0.5}V_{0.5}$LDHs-catalyzed OER in 1 M KOH + c mM $NaVO_3$ (green line), (c) LSV, (d) average voltage (bar graph) and decay voltage (point plot) data (with error bar) during the stability test of CO_3^{2-}–Ni_2Fe_1LDHs-catalyzed OER in 1 M KOH (blue line), VO_3^-–Ni_2Fe_1LDHs-catalyzed OER in 1 M KOH + 0.32 mM $NaVO_3$ (red line), $Ni_2Fe_{0.5}V_{0.5}$LDHs-catalyzed OER in 1 M KOH (yellow line), VO_3^-–$Ni_2Fe_{0.5}V_{0.5}$LDHs-catalyzed OER in 1 M KOH + 0.64 mM $NaVO_3$ (green line), (e) 24 h stability test data at 80 °C, 400 mA cm^{-2} in the two-electrode system.

dissolution compared to CO_3^{2-} intercalation. This indicates that either VO_3^- as the intercalation in LDHs or as an additive in the electrolyte can help reduce catalyst dissolution. We then conducted *ex situ* Raman characterization on the powder samples of CO_3^{2-}–Ni_2Fe_1LDHs and VO_3^-–Ni_2Fe_1LDHs (Fig. 4a). The results reveal that CO_3^{2-}–Ni_2Fe_1LDHs exhibit an independent peak at 695 cm^{-1}, which corresponds to the C–O vibration peak originating from CO_3^{2-}.[15] VO_3^-–Ni_2Fe_1LDHs shows strong peaks at 757 cm^{-1} and 821 cm^{-1} attributed to the asymmetric V–O–V stretching vibrations characteristic of VO_3^-.[16] Both the LDHs exhibit peaks at about 480 cm^{-1} and 568 cm^{-1}, respectively. These peaks can be attributed to the motion of the Ni–O lattice modes and the 2nd order lattice mode within the β-Ni(OH)$_2$ structure (Table S3†).[17] While a wavenumber lower than 300 cm^{-1} is unrecognized because of the high background signal, it can still be seen that there is a peak at about 320 cm^{-1} for both the samples, which can be attributed to the Ni–OH

lattice mode within the β-Ni(OH)$_2$ structure, which is characteristic peak distinguished from the Ni(Fe)OOH structure. Additionally, comparing the peaks at about 480 cm^{-1}, we discovered that CO_3^{2-}–Ni_2Fe_1LDHs have higher wavenumbers (483 cm^{-1}), which means that the Ni–O bond within has weaker vibration intensity and leads to an increase in the bond length. This result strongly supports the analysis according to the XRD pattern above. Both of them indicate that the as-prepared CO_3^{2-}–Ni_2Fe_1LDHs have a close-packed structure, whereas VO_3^-–Ni_2Fe_1LDHs have a non-close-packed structure.

To further reveal the origin of superior activity and stability, *in situ* Raman spectra characterization was conducted. Fig. 4b illustrates the LSV curves of CO_3^{2-}–Ni_2Fe_1LDHs and VO_3^-–Ni_2Fe_1 LDHs with 1 M KOH or 1 M KOH + 0.32 mM $NaVO_3$ tested in the *in situ* Raman cell.

For both CO_3^{2-}–Ni_2Fe_1LDHs and VO_3^-–Ni_2Fe_1LDHs, when they were charged at the open-circuit potential (OCP), the

23450 | *J. Mater. Chem. A*, 2024, **12**, 23447–23453

This journal is © The Royal Society of Chemistry 2024

Fig. 3 XPS spectra of (a) Ni 2p of the stability tested CO_3^{2-}-Ni$_2$Fe$_1$LDHs and (b) VO_3^--Ni$_2$Fe$_1$LDHs in 1 M KOH + 0/0.16/0.32/0.48/0.64 mM NaVO$_3$ as the electrolyte, respectively, (c) upper graph is the summary of the binding energy of Ni 2p$_{3/2}$ of CO_3^{2-}-Ni$_2$Fe$_1$LDHs and VO_3^--Ni$_2$Fe$_1$LDHs after the stability OER test derived from (a) and (b), the blue and red straight line is the binding energy of Ni 2p$_{3/2}$ from untested CO_3^{2-}-Ni$_2$Fe$_1$LDHs and VO_3^--Ni$_2$Fe$_1$LDHs; the bottom graph is the average voltage of CO_3^{2-}-Ni$_2$Fe$_1$LDHs and VO_3^--Ni$_2$Fe$_1$LDHs tested in 50 mA cm^{-2} for 50 h, (d) dissolution of Ni/Fe in the electrolyte of CO_3^{2-}-Ni$_2$Fe$_1$LDHs and VO_3^--Ni$_2$Fe$_1$LDHs after the stability test.

characterization peaks of CO_3^{2-}-Ni$_2$Fe$_1$LDHs tested with or without the additive NaVO$_3$ (Fig. 4c and d) and VO_3^--Ni$_2$Fe$_1$LDHs tested without the additive NaVO$_3$ (Fig. 4e) turned to the low left-high right pattern (454 cm^{-1}/530 cm^{-1}), whereas the VO_3^--Ni$_2$Fe$_1$LDHs tested with NaVO$_3$ (Fig. 4f) turned to the high left-low right pattern (470 cm^{-1}/548 cm^{-1}). Comparing our data with the analysis results

from Bell group's *in situ* Raman characterization of the α/γ phase during the OER process,[18] former cases transfer from the β-Ni(OH)$_2$ to the β-NiOOH, and later cases transfer from the β-Ni(OH)$_2$ to the γ-NiOOH at OCP immediately. As observed from Fig. 4c and e, the peak pattern changes along with increasing potential (left peak strength increases), whereas Fig. 4d and f, the characteristic peaks
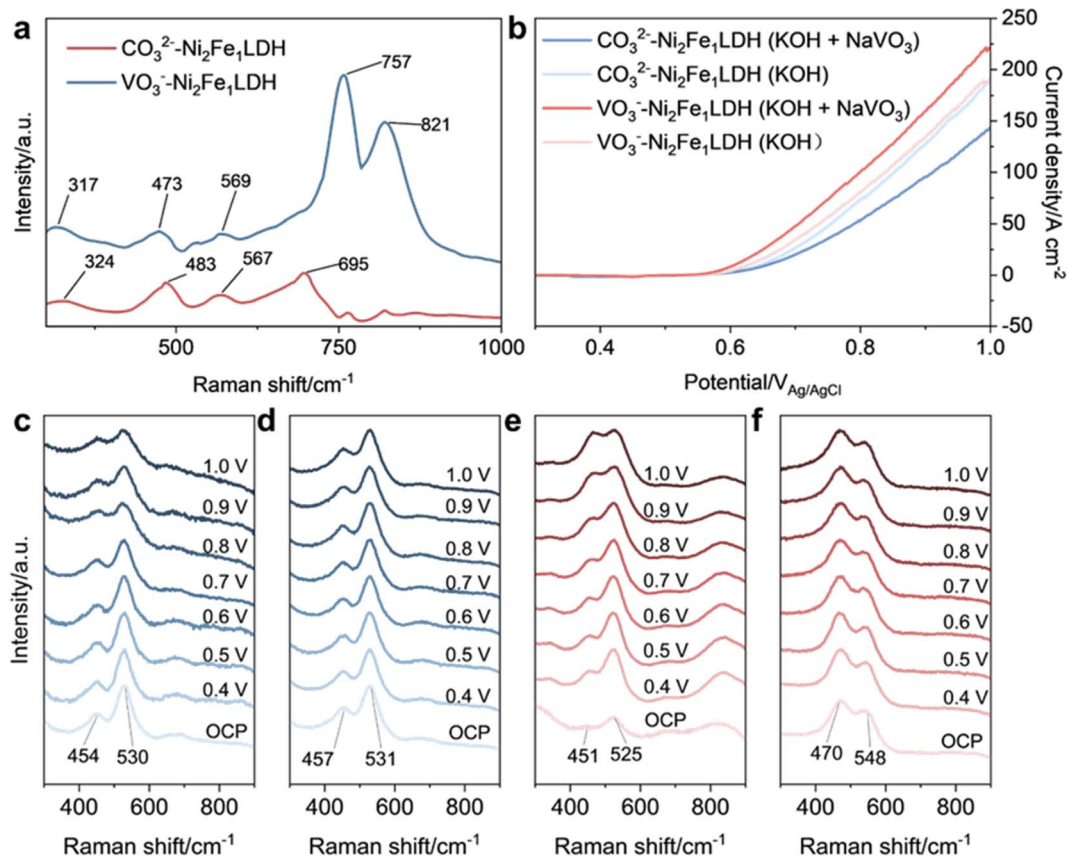
Fig. 4 (a) *Ex situ* Raman spectra of CO_3^{2-}-Ni$_2$Fe$_1$LDHs and VO_3^--Ni$_2$Fe$_1$LDHs, (b) OER polarization curves of CO_3^{2-}-Ni$_2$Fe$_1$LDHs (in 1 M KOH), CO_3^{2-}-Ni$_2$Fe$_1$LDHs (in 1 M KOH + 0.32 mM NaVO$_3$), VO_3^--Ni$_2$Fe$_1$LDH (in 1 M KOH) and VO_3^--Ni$_2$Fe$_1$LDHs (in 1 M KOH + 0.32 mM NaVO$_3$) tested in the Raman cell, *in situ* Raman spectra of (c) CO_3^{2-}-Ni$_2$Fe$_1$LDHs (in 1 M KOH), (d) CO_3^{2-}-Ni$_2$Fe$_1$LDHs (in 1 M KOH + 0.32 mM NaVO$_3$), (e) VO_3^--Ni$_2$Fe$_1$LDH (in 1 M KOH) and (f) VO_3^--Ni$_2$Fe$_1$LDH (in 1 M KOH + 0.32 mM NaVO$_3$).

This journal is © The Royal Society of Chemistry 2024

J. Mater. Chem. A, 2024, **12**, 23447–23453 | **23451**
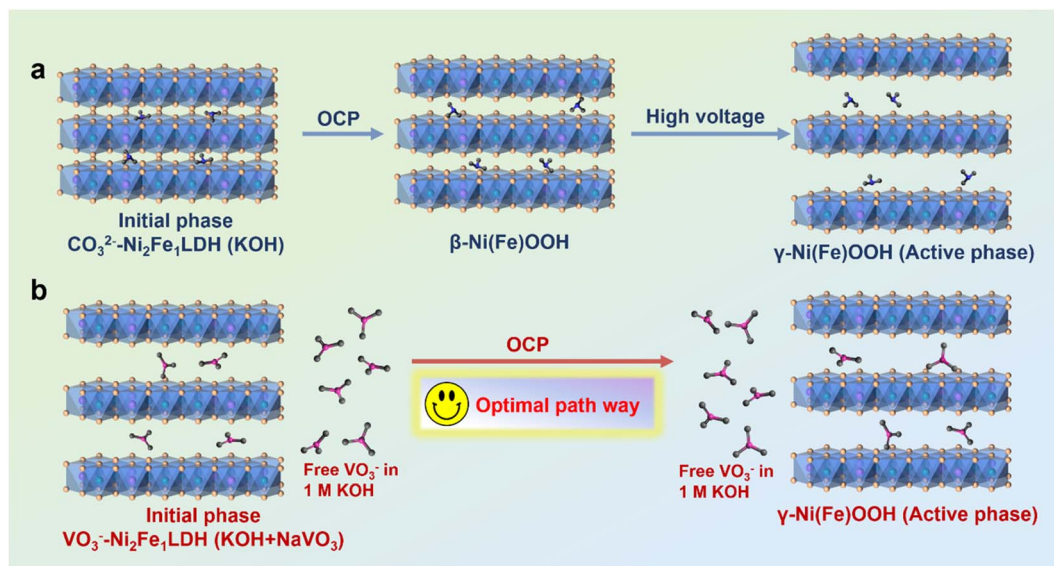
Fig. 5 Schematic diagram of two OER pathways of (a) CO_3^{2-}-Ni_2Fe_1LDHs (in 1 M KOH) and (b) VO_3^--Ni_2Fe_1LDHs (in 1 M KOH + 0.32 mM NaVO$_3$).

remain unchanged. This phenomenon indicates that the presence of VO_3^- in the electrolyte plays a key role in stabilizing the LDHs phase. Compared with Fig. 4c and e, it was found that when the potential reaches 1.0 $V_{Ag/AgCl}$, VO_3^--Ni_2Fe_1LDHs transforms the peak pattern to a flat left-right, but CO_3^{2-}-Ni_2Fe_1LDHs still maintains the peak pattern with the left peak slightly lower than the right peak, meaning that NiFe-LDHs with intercalated VO_3^- can more easily transition to the active γ-Ni(Fe)OOH.

Then, we compared the *in situ* Raman spectrum with (Fig. 4c) or without (Fig. 4f) these two effects above. When the voltage increased from 0.4 $V_{Ag/AgCl}$ to 0.6 $V_{Ag/AgCl}$, there is not much change observed in the peak intensity ratios of CO_3^{2-}-Ni_2Fe_1-LDHs, as shown in Fig. 4c. However, when the voltage > 0.7 $V_{Ag/AgCl}$, two characteristic peaks began transitioning from the low left-high right peak pattern to the flat left-right peak pattern. This evolution indicates that when LDHs start catalyzing OER at a higher voltage (0.6 V to 0.8 $V_{Ag/AgCl}$), it tends to transform from the β-phase to the γ-phase. As the voltage increases further, the ratio of peak heights remains constant, suggesting that it maintains a phase close to the active γ-Ni(Fe)OOH phase.[19] On the contrary, VO_3^--Ni_2Fe_1LDHs in alkaline electrolysis with 0.32 mM NaVO$_3$ (Fig. 4f) maintains the high left-low right Raman peak pattern (470 cm^{-1}/548 cm^{-1}) from the beginning to the end, which indicates that it is an active phase before OER occurs and its phase did not change in the whole process. Fig. 5 is a schematic diagram of phase transition of OER between the two samples, while Fig. 5b is the preferred shortcut path way, which eventually leads to the combination of VO_3^--Ni_2Fe_1LDHs with 0.32 mM NaVO$_3$ in the alkaline electrolyte that shows not only superior OER performance but also stability.

Conclusions

This work studies the effect of three vanadium-based species, namely, V^{III} in the laminates, VO_3^- as the intercalated anions

and VO_3^- as an additive in the electrolyte, on the OER performance of NiFe-LDHs at a high temperature and working current density. It was found that all the three strategies can improve the OER performance, but the best combination is VO_3^--Ni_2-Fe_1LDHs with 0.32 mM NaVO$_3$ in the alkaline electrolyte, which drops the overpotential by 119 mV compared with CO_3^{2-}-Ni_2-Fe_1LDHs without NaVO$_3$ in the electrolyte. The morphology characterization result revealed that the superior performance can be attributed to the looser layer spacing of VO_3^--Ni_2Fe_1-LDHs with the bigger interlayer anion VO_3^-, which facilitates active phase formation during OER. *In situ* Raman spectra analysis indicated that VO_3^- in electrolysis played a crucial role in stabilizing the phase of LDHs during the OER process. This study presents a novel approach for improving the design of water splitting anode catalysts to tolerate high temperature and high current density stability test as well as providing a new insight on electrolyte modification, helping to get a wider perspective of the way to promote hydrogen energy in the future. Among the transition metals, other variable metals besides vanadium can also participate in the process of OER catalyzed by NiFeLDHs as oxoates and metal cations. We expect to see more relevant experiments in subsequent studies to help the high-temperature electrolysis of water to further stabilize.

Data availability

Data available on request from the authors. The data that support the findings of this study are available from the corresponding author upon reasonable request.

Author contributions

X. S. conceived the idea. X. S. and D. Z. designed the experiment. M. M. and Y. Z. conducted the experiment. X. S. and D. Z. checked the data and got involved in the analysis,

discussion. W. L., X. D., J. J. and L. J. assisted in the experiment and data analysis. X. S., D. Z. and M. M. wrote the manuscript draft. All the authors approved the final version of the manuscript.

Conflicts of interest

There are no conflicts to declare.

Acknowledgements

References

1 (*a*) W. Zhang, M. Liu, X. Gu, Y. Shi, Z. Deng and N. Cai, *Chem. Rev.*, 2023, **123**, 7119; (*b*) J. Zhang, H. B. Yang, D. Zhou and B. Liu, *Chem. Rev.*, 2022, **122**, 17028; (*c*) Z. Zhou, Z. Pei, L. Wei, S. Zhao, X. Jian and Y. Chen, *Energy Environ. Sci.*, 2020, **13**, 3185; (*d*) S. Zhang, P. Du and X. Lu, *Sci. China Mater.*, 2024, **67**, 1379; (*e*) C. Liu, K. Xiong, X. Chena and X. Huang, *Sci. China Mater.*, 2023, **21**, 137.

2 (*a*) X. Wang, H. Zhong, S. Xi, W. S. V. Lee and J. Xue, *Adv. Mater.*, 2022, **34**, 2107956; (*b*) L. An, C. Wei, M. Lu, H. Liu, Y. Chen, G. G. Scherer, A. C. Fisher, P. Xi, Z. J. Xu and C.-H. Yan, *Adv. Mater.*, 2021, **33**, 2006328; (*c*) Z. Li, L. Sun, Y. Zhang, Y. Han, W. Zhuang, L. Tian and W. Tan, *Coord. Chem. Rev.*, 2024, **510**, 215837; (*d*) X. Zhang, J. Shao, W. Huang and X. Dong, *Sci. China Mater.*, 2018, **61**, 1143.

3 (*a*) H. Sun, X. Xu, H. Kim, Z. Shao and W. Jung, *InfoMat*, 2024, **6**, e12494; (*b*) X. Li, X. Hao, A. Abudula and G. Guan, *J. Mater. Chem. A*, 2016, **4**, 11973; (*c*) J. Xu, H. Jin, T. Lu, J. Li, Y. Liu, K. Davey, Y. Zheng and S.-Z. Qiao, *Sci. Adv.*, 2023, **9**, eadh1718; (*d*) H. Liu, Z. Zhang, J. Fang, M. Li, M. G. Sendeku, X. Wang, H. Wu, Y. Li, J. Ge, Z. Zhuang, D. Zhou, Y. Kuang and X. Sun, *Joule*, 2023, **7**, 558; (*e*) Y. Xue, J. Fang, X. Wang, Z. Xu, Y. Zhang, Q. Lv, M. Liu, W. Zhu and Z. Zhuang, *Adv. Funct. Mater.*, 2021, **31**, 2101405; (*f*) H. Wu, Q. Lu, Y. Li, J. Wang, Y. Li, R. Jiang, J. Zhang, X. Zheng, X. Han, N. Zhao, J. Li, Y. Deng and W. Hu, *Nano Lett.*, 2022, **22**, 6492.

4 H. J. Kim, S. H. Kim, S.-W. Kim, J.-K. Kim, C. Cao, Y. Kim, U. Kim, G. Lee, J.-Y. Choi, H.-S. Oh, H.-C. Song, W. J. Choi, H. Park and J. M. Baik, *Nano Energy*, 2023, **105**, 108003.

5 Y. Zhao, X. F. Lu, Z.-P. Wu, Z. Pei, D. Luan and X. W. D. Lou, *Adv. Mater.*, 2023, **35**, 2207888.

6 (*a*) Y. Chen, Y. Liu, W. Zhai, H. Liu, T. Sakthivel, S. Guo and Z. Dai, *Adv. Energy Mater.*, 2024, 2400059; (*b*) R. Chen, S.-F. Hung, D. Zhou, J. Gao, C. Yang, H. Tao, H. B. Yang, L. Zhang, L. Zhang, Q. Xiong, H. M. Chen and B. Liu, *Adv. Mater.*, 2019, **31**, 1903909; (*c*) D. J. Zhou, P. S. Li, X. Lin, A. Mckinley, Y. Kuang, W. Liu, W.-F. Lin and X. M. Sun, *Chem. Soc. Rev.*, 2021, **50**, 8790.

7 (*a*) H. Yang, C. Wang, Y. Zhang and Q. Wang, *Sci. China Mater.*, 2019, **62**, 681; (*b*) M. Yua, J. Zhenga and M. Guo, *Sci. China Mater.*, 2022, **20**, 472.

8 (*a*) P. Li, X. Duan, Y. Kuang, Y. Li, G. Zhang, W. Liu and X. Sun, *Adv. Energy Mater.*, 2018, **8**, 1703341; (*b*) J. Jiang, F. Sun, S. Zhou, W. Hu, H. Zhang, J. Dong, Z. Jiang, J. Zhao, J. Li, W. Yan and M. Wang, *Nat. Commun.*, 2018, **9**, 2885; (*c*) Y. Yang, L. Dang, M. J. Shearer, H. Sheng, W. Li, J. Chen, P. Xiao, Y. Zhang, R. J. Hamers and S. Jin, *Adv. Energy Mater.*, 2018, **8**, 1703189; (*d*) S. Deka, K. Jarswal, P. Rajput and B. Choudury, *J. Mater. Chem. A*, 2024, **12**, 9532.

9 (*a*) L. Guo, F. Zhang, J.-C. Lu, R.-C. Zeng, S.-Q. Li, L. Song and J.-M. Zeng, *Front. Mater.*, 2018, **12**, 198; (*b*) V. Murthy, H. D. Smith, H. Zhang and S. C. Smith, *J. Phys. Chem. A*, 2011, **115**, 13673; (*c*) V. R. Choudhary, J. R. Indurkar, V. S. Narkhede and R. Jha, *J. Catal.*, 2004, **227**, 257.

10 D. J. Zhou, Z. Cai, Y. M. Bi, W. L. Tian, M. LUO, Q. Zhang, Q. X. Xie, J. D. Wang, Y. P. Li, Y. Kuang, X. Duan, M. Bajdich, S. Siahrostami and X. M. Sun, *Nano Res.*, 2018, **11**, 1358.

11 R. Zhao, S. Xu, D. Liu, L. Wei, S. Yang, X. Yan, Y. Chen, Z. Zhou, J. Su, L. Guo and C. Burda, *Appl. Catal., B*, 2023, **338**, 123027.

12 X. Duan, M. Sendeku, D. Zhang, D. Zhou, L. Xu, X. Gao, A. Chen, Y. Kuang and X. Sun, *Acta Phys.-Chim. Sin.*, 2024, **40**, 2303055.

13 L. Chen, R. Deng, S. Guo, Z. Yu, H. Yao, Z. Wu, K. Shi, H. Li and S. Ma, *Front. Chem. Sci. Eng.*, 2023, **17**, 102.

14 F. Dionigi and P. Strasser, *Adv. Energy Mater.*, 2016, **6**, 1600621.

15 S. J. Palmer, T. Nguyen and R. L. Frost, *J. Raman Spectrosc.*, 2007, **38**, 1602.

16 S. Seetharaman, H. L. Bhat and P. S. Narayanan, *J. Raman Spectrosc.*, 1983, **14**, 401.

17 (*a*) B. C. Cornilsen, X. Y. Shan and P. L. Loyselle, *J. Power Sources*, 1990, **29**, 453; (*b*) W. Lai, L. H. Ge, H. M. Li, Y. L. Deng, B. Xu, B. Ouyang and E. Kan, *Int. J. Hydrogen Energy*, 2021, **46**, 26861.

18 B. S. Yeo and A. T. Bell, *J. Phys. Chem. C*, 2012, **116**, 8394.

19 L. Trotochaud, S. L. Young, J. K. Ranney and S. W. Boettcher, *J. Am. Chem. Soc.*, 2014, **136**, 6744.

This journal is © The Royal Society of Chemistry 2024

J. Mater. Chem. A, 2024, **12**, 23447–23453 | **23453**